



HAL
open science

Seven-year monitoring of mercury in wet precipitation and atmosphere at the Amsterdam Island GMOS station

Antonella Tassone, Olivier Magand, Attilio Naccarato, Maria Martino, Domenico Amico, Francesca Sprovieri, Hippolyte Leuridan, Yann Bertrand, Michel Ramonet, Nicola Pirrone, et al.

► To cite this version:

Antonella Tassone, Olivier Magand, Attilio Naccarato, Maria Martino, Domenico Amico, et al.. Seven-year monitoring of mercury in wet precipitation and atmosphere at the Amsterdam Island GMOS station. *Heliyon*, 2023, 9 (3), pp.e14608. 10.1016/j.heliyon.2023.e14608 . hal-04037485v1

HAL Id: hal-04037485

<https://hal.science/hal-04037485v1>

Submitted on 20 Mar 2023 (v1), last revised 24 Mar 2023 (v2)

HAL is a multi-disciplinary open access archive for the deposit and dissemination of scientific research documents, whether they are published or not. The documents may come from teaching and research institutions in France or abroad, or from public or private research centers.

L'archive ouverte pluridisciplinaire **HAL**, est destinée au dépôt et à la diffusion de documents scientifiques de niveau recherche, publiés ou non, émanant des établissements d'enseignement et de recherche français ou étrangers, des laboratoires publics ou privés.

Journal Pre-proof

Seven-year monitoring of mercury in wet precipitation and atmosphere at the Amsterdam Island GMOS station

Antonella Tassone, Olivier Magand, Attilio Naccarato, Maria Martino, Domenico Amico, Francesca Sprovieri, Hippolyte Leuridan, Yann Bertrand, Michel Ramonet, Nicola Pirrone, Aurelien Dommergue

PII: S2405-8440(23)01815-7

DOI: <https://doi.org/10.1016/j.heliyon.2023.e14608>

Reference: HLY 14608

To appear in: *HELIYON*

Received Date: 20 December 2022

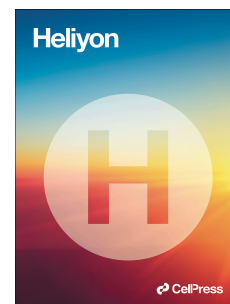
Revised Date: 5 March 2023

Accepted Date: 13 March 2023

Please cite this article as: , Seven-year monitoring of mercury in wet precipitation and atmosphere at the Amsterdam Island GMOS station, *HELIYON* (2023), doi: <https://doi.org/10.1016/j.heliyon.2023.e14608>.

This is a PDF file of an article that has undergone enhancements after acceptance, such as the addition of a cover page and metadata, and formatting for readability, but it is not yet the definitive version of record. This version will undergo additional copyediting, typesetting and review before it is published in its final form, but we are providing this version to give early visibility of the article. Please note that, during the production process, errors may be discovered which could affect the content, and all legal disclaimers that apply to the journal pertain.

© 2023 Published by Elsevier Ltd.

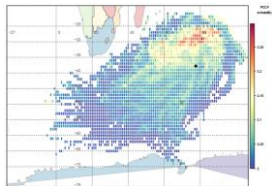
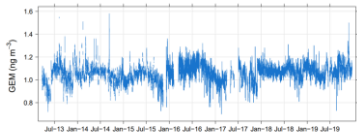


CRediT Authorship contribution statement

Antonella Tassone: Conceptualization of the study, preparation of material for sampling, laboratory Hg analysis, data analysis, original manuscript writing; **Olivier Magand:** Implementation of Hg measurements at TAAF-IPEV Amsterdam Island district, observations monitoring management, field campaign, data treatment qualification and validation, IPEV GMOS_{Stral-1028} and Hg dataset AERIS (GMOS-FR national database <https://gmos.aeris-data.fr/>) program managing, funding acquisition, original manuscript writing; **Attilio Naccarato:** Conceptualization of the study, supervision and coordination of the work, original manuscript writing, funding acquisition and project managing; **Maria Martino:** Preparation of material for sampling, laboratory Hg analysis, data analysis; **Domenico Amico:** Preparation of material for sampling, laboratory Hg analysis, data analysis; **Francesca Sprovieri:** Manuscript review and editing, funding acquisition and project managing, GMOS network coordination; **Hippolyte Leuridan:** ICOS station management at Amsterdam Island; **Yann Bertrand:** IPEV GMOS_{Stral-1028} field campaign on THg in precipitation; THg collector system maintenance; **Michel Ramonet:** ICOS station management at Amsterdam Island; **Nicola Pirrone:** Funding acquisition and project managing, GMOS network coordination; **Aurelien Dommergue:** Implementation of Hg measurements at TAAF-IPEV Amsterdam Island district, funding acquisition. All co-authors contributed to data interpretation, reviewing, and editing the manuscript.



2013 – 2019 monitoring
of GEM and total Hg
in wet deposition



1 **Seven-year monitoring of mercury in wet precipitation and atmosphere at the Amsterdam**
2 **Island GMOS station**

3
4 Antonella Tassone^{1*}, Olivier Magand², Attilio Naccarato^{1,3}, Maria Martino¹, Domenico Amico¹,
5 Francesca Sprovieri¹, Hippolyte Leuridan⁴, Yann Bertrand², Michel Ramonet⁴, Nicola Pirrone¹
6 and Aurelien Dommergue²

7
8
9
10 1 CNR-Institute of Atmospheric Pollution Research (CNR-IIA), Rende, Italy

11 2 Institut des Géosciences de l'Environnement, Univ. Grenoble Alpes, CNRS, IRD, Grenoble INP,
12 38400 Grenoble, France

13 3 Department of Chemistry and Chemical Technologies, University of Calabria, Via P. Bucci,
14 Rende, Italy

15 4 Laboratoire des Sciences du Climat et de l'Environnement, LSCE-IPSL (CEA-CNRS-UVSQ),
16 Université Paris-Saclay, 91191 Gif-sur-Yvette, France

17
18
19
20 *Corresponding author:

21 Antonella Tassone

22 CNR-Institute of Atmospheric Pollution Research, Rende, Italy

23 e-mail: antonella.tassone@iia.cnr.it

Abstract

Mercury (Hg) fate and transport research requires more effort to obtain a deep knowledge of its biogeochemical cycle, particularly in the Southern Hemisphere and Tropics that are still missing of distributed monitoring sites.

Continuous monitoring of atmospheric Hg concentrations and trend worldwide is relevant for the effectiveness evaluation of the Minamata Convention on Mercury (MCM) actions. In this context, Gaseous Elemental Mercury (GEM) and total mercury (THg) in precipitations were monitored from 2013 to 2019 at the Amsterdam Island Observatory (AMS - 37°48'S, 77°34'E) to provide insights into the Hg pathway in the remote southern Indian Ocean, also considering ancillary dataset of Rn-222, CO₂, CO, and CH₄. GEM average concentration was 1.06 ± 0.07 ng m⁻³, with a slight increase during the austral winter due to both higher wind speed over the surface ocean and contributions from southern Africa. In wet depositions, THg average concentration was 2.39 ± 1.17 ng L⁻¹, whereas the annual flux averaged 2.04 ± 0.80 μg m⁻² yr⁻¹. In general, both GEM and Volume-Weighted Mean Concentration (VWMC) of THg did not show an increasing/decreasing trend over the seven-year period, suggesting a substantial lack of evolution about emission of Hg reaching AMS.

Air masses Cluster Analysis and Potential Source Contribution Function showed that oceanic evasion was the main Hg contributor at AMS, while further contributions were attributable to long-range transport events from southern Africa, particularly when the occurrence of El Niño increased the frequency of wildfires.

Keywords: Wet deposition flux; Southern Hemisphere; Atmospheric pollution; Source identification; Atmospheric transport; Mercury measurements

51 **1. Introduction**

52 Due to its toxicity and great impact on human health and the environment, mercury (Hg) has
53 increasingly been investigated by the scientific community [1,2] with the overall aim to reduce
54 its emissions in each environmental compartment [3]. The Minamata Convention on Mercury
55 (MCM) is perhaps the most important international regulatory framework aimed at protecting
56 human health and the environment from anthropogenic emissions of Hg and its compounds [4]
57 and the effectiveness evaluation of its actions has highlighted the need to increase the number of
58 ground-based monitoring sites worldwide, particularly in areas of scarce data coverage and to
59 provide comparable Hg data both in the background and in impacted areas [5]. This complex
60 framework draws attention to the need for multiple analytical methods and the exploitation of
61 new analytical strategies for comprehensive investigations, which should also include remote
62 areas [6–9].

63 Although several Hg monitoring programs and networks have been established over the years,
64 [10–13] the monitoring stations that provide Hg data both in air and wet depositions in the open
65 ocean and remote areas are still limited in number [8,10,14–24] particularly in the Southern
66 Hemisphere.

67 In this context, the station on Amsterdam Island (AMS) has been set up in the framework of the
68 Global Mercury Observation System (GMOS) Hg global network (<http://www.gmos.eu/>), with
69 the support of the French Polar Institute (IPEV). The unique geographic location of this site has
70 enabled the study of background data on major air pollutants in the Southern Hemisphere due to
71 the absence of local anthropogenic sources and its distance from maritime traffic routes
72 [15,17,25–29].

73 The present manuscript is an updated study on the temporal variability of Gaseous Elemental
74 Mercury (GEM) and total Hg (THg) in precipitations from 2013 to 2019 at AMS providing new
75 insights into the Hg pathway in the Southern Hemisphere. The investigation of seasonal and inter-
76 annual variability, combined with the analysis of CO₂, CO, CH₄, and radon-222 (Rn-222) data,

77 with the support of Potential Source Contribution Function (PSCF) and Cluster Analysis (CA),
78 permitted to assess the evolutionary tendencies of Hg at the Southern Hemisphere midlatitudes
79 and pinpoint the potential sources associated with long-range transport and El Niño Southern
80 Oscillation (ENSO).

81 **2. Materials and methods**

82 **2.1 Sampling site**

83 Amsterdam Island (37.7983° S, 77.5378° E) is a small remote volcanic island of 55 km² in the
84 southern Indian Ocean, 3200 km from Australia, 3400 km from Madagascar, 4200 km from South
85 Africa, and 3300 km from Antarctica. The atmospheric observatory of Pointe Benedicte is
86 northwest to the island at an altitude of 55 m above sea level, and due to its strategic position that
87 ensures minimal local interference, the station is of particular interest to study Hg dynamics and
88 pathway under unique background conditions.

89 Within the GMOS global network, it has been classified as a master site [11] and it is also part of
90 other atmospheric monitoring programs such as the Global Atmosphere Watch World
91 Meteorological Organization (GAW WMO), the French national monitoring system Integrated
92 Carbon Observation System ICOS-France-Atmosphere for the long-term observation of
93 greenhouse gases (GHGs), and the Global Observation System for Mercury (GOS⁴M) GEO
94 Flagship [10,16,17]. A more detailed description of the site is given in the Supporting Information
95 (Text S1).

96 **2.2 Meteorological variables and CO₂, CO, CH₄, and Rn-222 measurements**

97 Meteorological data – air temperature, rainfall amount, wind speed and direction – were provided
98 by the local meteorological station. The dataset of GHGs included CO₂, CO, and CH₄ from March
99 23, 2013, to December 22, 2019. A temporal gap exists in the CO measurements, which started
100 from December 2, 2015. CO₂, CO, and CH₄ were monitored using Picarro gas analyzers, which
101 used cavity ring-down spectroscopy to measure the gas concentration every 30 seconds with a
102 precision (1 sigma confidence) for hourly measurements of 10 ppb, 1 ppb, and 0.3 ppb,

103 respectively, in compliance with the specifications of the manufacturer. Calibration was performed
104 monthly. The raw data were manually checked and validated by ICOS staff [30], before being
105 hourly averaged.

106 Radon-222 measurements, covering the same period considered for GHGs, were performed using
107 an alpha spectrometer which required monthly calibration and ensured a minimum detected
108 activity of about 10 mBq m^{-3} with an uncertainty of about 40%.

109 This set of ancillary data proved useful to track continental air over the ocean [31]. Indeed, Rn-
110 222 concentration at AMS exceeding the threshold of 80 mBq m^{-3} (i.e., radonic storms), indicated
111 that the air mass over the island recently passed over the mainland, usually southern Africa [17,32].

112 The time series of all gases were analyzed on an hourly, seasonal, and annual basis, with seasonal
113 boundaries defined as follows: austral winter from July to September, austral summer from
114 December to February, intermediate season 1 (IS1) from March to June, and intermediate season
115 2 (IS2) from October to November. This classification revealed useful since the meteorological
116 conditions in June are more similar to that in the preceding months than in July–August, as also
117 the case of other sites in the Southern Hemisphere, and more strictly in Africa [33].

118 **2.3 Mercury determination in the atmosphere and wet deposition**

119 **2.3.1 GEM measurements**

120 GEM was continuously measured from March 23, 2013, to December 22, 2019, using Tekran
121 analyzer 2537A/B models (Tekran Inc., Toronto, Canada) based on amalgamation onto dual gold
122 cartridge design, thermal desorption, and quantification by cold vapor atomic fluorescence
123 spectroscopy (CV-AFS). Calibration was performed using both the internal permeation sources
124 (every 69 h) and manual injections of saturated Hg vapor (every year). To ensure comparability of
125 the Hg data, GEM measurements were carried out according to GMOS Standard Operating
126 Procedures (SOPs) [34].

127 **2.3.2 Rainwater sampling and total mercury quantification**

128 Wet deposition samples were continuously collected from March 24, 2013, using an automatic
129 wet-only NSA-171 Eigenbrodt collector which comprises a glass funnel connected to a 1-L
130 fluorinated high-density polyethylene (FLPE) bottle. The entire sampling apparatus was
131 thoroughly acid-cleaned, according to the procedures reported by Tassone et al. [35], based on the
132 SOPs developed within the GMOS network [36]. Each deployment lasted 6-45 days, depending
133 on the season (wet or dry) and according to exceptional periods of intense rainfall events. Analyses
134 of wet deposition samples were performed at the CNR-IIA laboratories following the US-EPA
135 method 1631E guidance reported in the literature [35]. Quality assurance/quality control (QA/QC)
136 procedures were routinely implemented, including the analysis of duplicate samples, accuracy test
137 using certified reference material (NIST1641), matrix spikes, and assessment of Hg contamination
138 through the analysis of the system, transport, reagent and field blanks (more details in Text S2).

139 **2.4 Data treatment**

140 Raw GEM time series were quality-controlled according to GMOS SOPs, using a dedicated
141 software developed at the Institute of Environmental Geosciences (<https://doi.org/10.25326/168>
142 available at <https://gmos.aeris-data.fr>, last access: 10 February 2023) [37]. Specifically, the
143 QA/QC procedure involved comparing the raw data with fixed criteria, concerning both the
144 calibration and the readout steps of airborne measurements [34].

145 THg values were derived according to UNI 15853:2010 and converted into volume-weighted mean
146 concentration (VWMC) values, while seasonal and annual Hg wet deposition fluxes (F_w) were
147 calculated as reported in Sprovieri et al. [10] by using the seasonal/yearly VWMCs and cumulative
148 rain depths (P^i , mm), according to Eq. (1):

$$149 \quad F_w = VWMC_{Hg} \sum_{i=1}^n P^i / 1000 \quad (1)$$

150 The statistical significance of temporal variability of each variable was determined using linear
151 regression with the method of Pearson's correlation coefficient and the differences in annual and
152 seasonal concentration values were investigated using Mann-Whitney and ANOVA tests.

153 The seasonal Mann-Kendall trend test was applied to monthly mean data of each variable, after
154 verification of their significant seasonality using the Kruskal-Wallis test, to detect trends while
155 Sen's slope estimator was applied to assess their magnitude, using the Theil-Sen method [38].

156 The investigation of the impact of El Niño on Amsterdam Island was conducted using cross-
157 correlation to seek lag times between the Southern Oscillation Index (SOI), as a tracer of El Niño
158 occurrence, and GEM and CO concentrations. All data analyses were performed using the R
159 software.

160 **2.5 Backward trajectories and source identification techniques**

161 The interpretation of the surveyed time series was carried out using the U.S. NOAA's HYbrid
162 Single-Particle Lagrangian Integrated Trajectory (HYSPLIT) model
163 (<http://ready.arl.noaa.gov/HYSPLIT.php>, last access: May 3, 2022), which permitted to obtain
164 information on the path of air masses to the receptor site. For this purpose, the READY website
165 was used to compute 5-day back-trajectories, at 3-hour intervals, at 50 m above ground level in
166 the domain 70° - 0° S and 0° - 120° E [33,39,40]. Considering the remoteness of the island, 5-day
167 trajectories may be deemed short for tracing possible Hg sources reaching AMS. However, longer
168 trajectories calculated for the entire 7-year monitoring period would have entailed a higher
169 computational cost. We therefore calculated 10-day trajectories only for few cases, in order to
170 support our findings overcoming computational limitations. More specifically, 10-day trajectories
171 were used to facilitate the interpretation of particularly high or low values of GEM and Rn as well
172 as to run the CA. The GDAS $1^{\circ}\times 1^{\circ}$ from the Global Data Assimilation System was selected as the
173 meteorological dataset [41].

174 In addition, CA was applied to group air masses according to their origin through the computation
175 of the proportion of time that a particular back-trajectory was in a specific wind sector (e.g., S,
176 SW, W). CA was performed using Ward's Minimum-Variance method which, starting with groups
177 containing single trajectories, iteratively merges pairs of them so as to obtain the minimum
178 increase in the sum of squared distances between the members and the centroids of the

179 corresponding groups, summed over the resulting groups [42–44]. The centroid of the newly-
180 formed group, i.e., our mean trajectory, is recomputed each time using the data from the individual
181 groups previously separated, before calculating the squared distances [45]. In our study, an angle
182 distance matrix was used to assess the similarity between the trajectories to be merged. The optimal
183 number of clusters was chosen following the total spatial variance (TSV) metric in the Elbow
184 method [45,46], selecting a variance criterion of 20%. This approach relies on calculating the sum
185 of the spatial variance of all the clusters, until TSV increases significantly, thus indicating that the
186 merged clusters are not very similar. This increase in TSV denotes the completion of the clustering
187 process [47], and in our case, it resulted in four clusters as the optimal number. Furthermore, a
188 hybrid receptor model, namely the Potential Source Contribution Function, was used to locate
189 potential emission sources around the receptor site [48,49]. This technique assumes that air masses
190 that intercept emission sources in the grid cell (i, j) can get enriched in the pollutants emitted by
191 that source and transport them to the receptor site. The PSCF is defined by Eq. (2):

$$192 \quad PSCF = \frac{m_{ij}}{n_{ij}} \quad (2)$$

193 where n_{ij} is the number of times that the trajectories passed through the cell and m_{ij} is the number
194 of times that a source concentration was high (>90th percentile) when the trajectories passed
195 through the cell (i, j). The cell with the higher PSCF value thereby characterizes the most likely
196 source location.

197 **3. Results and discussion**

198 **3.1 Variability of CO₂, CO, CH₄, Rn, and meteorological conditions**

199 The summary of the annual meteorological variables and atmospheric gases is listed in Table 1.
200 The monthly median air temperature ranged from 11 °C in winter to 19 °C in summer (Fig. S1)
201 while winds mainly blew from NNW to WSW, without significant differences in direction among
202 the seasons (Fig. S1), except for a higher frequency of N-NW air masses during winter. The most
203 abundant precipitations were measured during IS1 except for 2013, when the maximum was

204 recorded during winter (Fig. 1). On an annual basis, rainfall averaged 905 ± 62 mm and varied
205 between 833 mm, collected in 2013, and 1003 mm, in 2019.

206 The measured CO_2 ($n=56976$, 89.5% of available hourly data) showed a statistically significant
207 increase over the investigated period, from 390.5 ppm in 2013 to 412.8 ppm in 2019 (Fig. S2),
208 with an average rate of $2.46 \text{ ppm year}^{-1}$ ($p<0.05$), thus confirming the growing trend already found
209 in previous studies [26]. Daily CO_2 concentration showed little variability among the seasons,
210 with a slight decrease between 9 a.m. and 6 p.m., suggesting a weak influence from the
211 photosynthetic activity of local vegetation (Fig. S2).

212 The hourly CO values ($n=34264$, 88% of available data) ranged from 30 ppb to a maximum of 65
213 ppb (Fig. S3), with an upward significant trend ($p<0.05$), as confirmed by the positive Sen's slope
214 value, which was $6.8\text{e-}05 \text{ ppb year}^{-1}$. However, it is worth noticing that this increasing tendency
215 was very small, thus not physically meaningful. On a seasonal basis, a clear distribution was
216 observed, with the lowest values being obtained in February and March (Fig. S3), due to removal
217 phenomena favored by the high presence of radical OH during IS1. Conversely, these removal
218 processes were weak during winter and the CO concentration increased significantly, with maxima
219 in October [50]. In addition, between June and October, this pattern was probably influenced by
220 the long-range transport of CO released during the biomass burning events in southern Africa [51].

221 The hourly CH_4 values (Fig. S4) showed a statistically significant increase from 1747 ppb to 1841
222 ppb with an average value of 1794 ± 21 ppb ($n=56964$, 89.5% of available hourly data) and a
223 growth rate of $8.5 \text{ ppb year}^{-1}$ ($p<0.05$). The lowest values were recorded in January-April (Fig. S4)
224 and were mainly due to the reaction with OH radicals, as was also observed for CO. Indeed, CH_4
225 and CO showed a significant correlation ($r=0.57$, $p<0.05$) over the covered period, suggesting that
226 common mechanisms have driven their pattern on a seasonal scale [50,52,53].

227 The 2-hour Rn-222 activity was on average $35.36 \pm 32.24 \text{ mBq m}^{-3}$ ($n=26988$, 92.3% of available
228 data) with a maximum of $398.80 \text{ mBq m}^{-3}$ (Fig. S5). The Mann-Kendall test revealed a significant
229 decrease that was confirmed by the Sen's slope value ($-4.1\text{e-}04 \text{ mBq m}^{-3} \text{ year}^{-1}$). However, this

230 tendency was quite small, therefore not physically meaningful, as in the case of CO. Annual Rn
231 activities (Fig. S5) ranged between 24.93 ± 26.78 mBq m⁻³ (in 2016) and 48.10 ± 19.4 mBq m⁻³
232 (in 2013), as typical for marine air masses which usually range between 30-50 mBq m⁻³ [27,54,55].
233 Radonic storms from southern Africa were mainly detected during winter (Fig. S5), which is the
234 season with the greatest contribution of the long-range transport [17]. Their continental origin was
235 confirmed by the correlation between Rn and CO, which improved when considering only the
236 biomass burning season (i.e., austral winter) rather than the entire period, with a 10-fold increase
237 in the correlation coefficient, from 0.02 to 0.20 ($p < 0.05$). Besides, by looking at the relationship
238 between Rn and wind direction (Fig. S5), it can be noticed a lower frequency of radonic storms
239 transported up to AMS during the second half of the investigated period. Although there was
240 substantial uniformity in the direction of Rn origin (WNW), these radonic storms decreased their
241 frequency from W over time, and in 2019 they were recorded only from the northernmost (NW)
242 sectors.

243 **3.2 Hg in the atmosphere and wet deposition**

244 **3.2.1 GEM measurements**

245 The individual mean hourly GEM values from March 2013 to December 2019 (Fig. 2) ranged
246 from 0.70 to 1.58 ng m⁻³, resulting in a mean concentration of 1.06 ± 0.07 ng m⁻³ ($n=45018$, 70.7%
247 of available data), which is comparable with the concentrations (0.9-1.0 ng m⁻³) usually found at
248 background sites of the Southern Hemisphere [11]. The observed GEM was also consistent with
249 previous measurements at AMS, which reported concentrations of 1.03 ng m⁻³ [17] and 1.05 ng
250 m⁻³ [16], as well as at the Cape Point station in southern Africa, where the annual mean GEM was
251 1.09 ng m⁻³ [16]. However, concentrations at AMS were slightly higher than in other subequatorial
252 sites, such as the EMMA station in Argentina, where the average concentration was 0.9 ng m⁻³
253 [22], and the Cape Grim station in Tasmania, where concentrations of 0.9-1.0 ng m⁻³ were found
254 [56,57]. On a seasonal basis (Fig. 2), we recorded a slightly but significantly higher Hg
255 concentration in winter than in summer (1.08 ± 0.05 vs. 1.06 ± 0.07 ng m⁻³, $p < 0.05$). This seasonal

256 variability may be ascribed to the impact of the Intertropical Convergence Zone (ITCZ) shift
257 during the austral winter, which caused changes in the wind speed on the sea surface [58], thus
258 favoring Hg emission. Indeed, ITCZ is a belt of air masses from both the Northern and Southern
259 hemispheres mixing together which crosses the equator from south to north around April-May
260 (IS1) and reaches its northernmost point around June-July (winter), and then moves south again
261 around August-September [58,59]. Therefore, the relocation of the ITCZ over the Indian Ocean
262 was likely a vector of air masses from the north to AMS that reasonably influenced the recorded
263 GEM concentrations. In addition, a non-negligible contribution to the observed GEM seasonal
264 variability was the long-range transport from southern Africa during the biomass burning season,
265 that was confirmed by the significant positive correlation between GEM and CO only in winter
266 ($r=0.28$, $p<0.05$), contrary to the findings regarding the correlations between GEM and CO₂ or
267 CH₄, which were in all cases non-significant.

268 **3.2.2 Total mercury in rainwater**

269 The annual-averaged VWMC of THg in precipitation samples ($n=27$) was 2.39 ± 1.17 ng L⁻¹ and
270 varied in the range from 1.16 ng L⁻¹ to 4.67 ng L⁻¹, which were obtained in 2015 and 2018,
271 respectively, when total rainfall was 916 mm and 855 mm (Table 1 and Fig. 1). On both a seasonal
272 and annual basis, the VWMC showed no significant increase or decrease over time, suggesting
273 that no substantial changes in the concentration of atmospheric oxidized Hg species during the
274 investigated period were observed. Since a significant source of these species at AMS is biomass
275 burning in southern Africa [16], it can be hypothesized that these emissions did not change during
276 the last decade.

277 Even focusing only on the winter seasons, when African air masses are detectable at AMS, we did
278 not observe a clear upward/downward tendency of VWMC, rather it was mostly fluctuating (Fig.
279 1). Except for 2016, the lowest values were observed during the rainy season, i.e., from May to
280 October, due to the movement of cold fronts from the west. Conversely, higher values were mainly
281 found in IS2 (Fig. 1), except for 2014 and 2017 when a peak was recorded during summer. In

282 particular, during IS2 2018 we observed a VWMC value of 10.93 ng L^{-1} , associated a rainfall
283 amount (199 mm) that was not notably different from the typically measured values. The analysis
284 of the wind roses combined with backward trajectories during IS2 2018 did not provide us with
285 immediate answers to this event. Within the same synoptic pattern, more intense winds from the
286 W and WNW sectors in IS2 than other seasons were recorded (Fig. S6), suggesting the potential
287 contribution of long-range transport from Africa. Therefore, we hypothesize during this season
288 some unusual emission phenomena occurred in Africa, whose oxidized Hg was then scavenged by
289 the wet deposition reaching AMS [60,61]. This hypothesis is supported by previous measurements
290 at AMS, which showed that the highest concentrations of particle-bound Hg were observed during
291 episodes of stronger winds from the NW sector [17].

292 The effect of washout of atmospheric oxidized Hg species from wet deposition was studied on a
293 seasonal basis by correlating VWMC with total rainfall ($n=27$, $r=-0.21$, $p>0.05$) (Fig. 3), which
294 resulted in a negative but not sufficient coefficient. The correlation was low because the occurrence
295 was observed by considering seasonal values from samples that averaged out their respective
296 contributions. Similarly, a non-significant correlation was found between GEM and wet deposition
297 volume ($n=27$, $r=0.11$, $p>0.05$), suggesting rainfall events did not affect GEM concentration (Fig.
298 3). As regards the VWMC and the corresponding seasonal GEM concentrations (Fig. 3), the
299 correlation study revealed a not significant linear relationship between the two forms ($n=27$,
300 $r=0.05$, $p>0.05$), which was probably due to their different temporal variability. Indeed, GEM
301 showed a quite stationary pattern compared to the more variable VWMC throughout the covered
302 period.

303 The values of VWMC in precipitation samples and their respective precipitation volumes resulted
304 in an average wet deposition flux of $2.04 \pm 0.80 \mu\text{g m}^{-2} \text{ year}^{-1}$, and therefore slightly higher than
305 the value of $1.95 \mu\text{g m}^{-2} \text{ year}^{-1}$ reported in a previous study [10]. This finding was impacted by the
306 higher value of Hg in wet deposition observed in 2018. In fact, during 2018 the highest wet

307 deposition flux was attained ($3.31 \mu\text{g m}^{-2} \text{ year}^{-1}$), whereas the lowest value ($1.06 \mu\text{g m}^{-2} \text{ year}^{-1}$)
308 resulted in 2015. On a seasonal scale, the maximum flux varied year-to-year between IS1 and IS2.
309 A positive significant correlation ($n=27, r=0.48, p<0.05$) was observed between the wet deposition
310 flux and associated rainfall (Fig. 3), indicating that wet Hg deposition flux increased with
311 increasing rainfall, as also reported in other studies showing that rainfall had a greater influence
312 on the variation of wet deposition fluxes [62].

313 The average THg (whence the HgII forms) wet deposition flux is lower than the GEOS-Chem
314 model results that produced wet Hg deposition flux around $5\text{-}6 \mu\text{g m}^{-2} \text{ year}^{-1}$ [63,64] in the areas
315 surrounding AMS. Compared with other models, such as GLEMOS, GEM-MACH-Hg, and
316 ECHMERIT, our experimental result was also lower, as can be seen from the spatial distribution
317 maps reported in Travnikov et al. [65], from which it can be inferred that the flux value in 2013
318 ranged in $2.9\text{-}4.4, 2.9\text{-}7.3, \text{ and } 4.4\text{-}7.3 \mu\text{g m}^{-2} \text{ year}^{-1}$, respectively. This model-to-measurement gap
319 outlines the importance of monitoring wet deposition at AMS to gather experimental results that
320 contribute to the study of the latitudinal gradient of HgII wet deposition over the oceans, hence
321 improving the understanding of Hg inputs to different ocean regions.

322 **3.3 Influence of the El Niño Southern Oscillation (ENSO)**

323 The El Niño Southern Oscillation (ENSO) is a cyclical meteorological event that occurs
324 approximately every 3-7 years and causes variation of rainfall amount with consequent impact on
325 emission phenomena, such as biomass burning due to long periods of drought [66–68]. The
326 occurrence of El Niño has usually been detected using atmospheric indexes like SOI (Southern
327 Oscillation Index), MEI (Multivariate ENSO Index), and ONI (Oceanic Niño Index).

328 From 2013-2019 (Fig. 4), ONI values reached very high levels between July 2015 and July 2016,
329 with a peak in December-January. MEI and SOI also showed a very similar, increasing trend over
330 the same period. However, the growth of all the indexes around 2016 was not accompanied by a
331 sharp and direct increase in GEM, suggesting at first a limited simultaneous influence of ENSO. ,
332 On the contrary, the highest GEM concentrations were observed at the most negative SOI values

333 on average 6-8 months after the El Niño event (Fig. S7). This result is in agreement with the
334 findings at Cape Point (South Africa) and Mace Head (Ireland) [67], therefore supporting the
335 influence of El Niño on GEM variability, which can occur with the increased wildfire frequency
336 (which also impacts CO concentration) [67] or with enhanced Hg re-emission from the ocean
337 surface caused by the increase of the sea surface temperature [69,70]. Huang and Zhang indeed
338 recently simulated by GEOS-Chem model a positive anomaly of atmospheric Hg concentration,
339 lagged of 3 months, driven by Hg(0) evasion fluxes after the occurrence of El Niño [71].

340 In our study, we found a significant cross correlation between CO and SOI, with lag time peaking
341 at 4-6 months (Fig. S7) comparable to that between GEM and SOI and therefore we suggest that
342 ENSO-modulated biomass burning was one of the major mechanisms of GEM variability on
343 Amsterdam Island.

344 **3.4 Backward trajectories analysis**

345 The analysis of the 10-day backward trajectories revealed that more than 30% of the GEM peaks
346 (concentration > 95th percentile) were associated with the transport of air masses coming from
347 southern Africa during the biomass burning season (Fig. S8). A similar apportionment was
348 confirmed for the high concentrations of Rn-222 (Fig. S8), whose pattern was mainly affected by
349 the emissions from the African continent. The 10-day trajectory analysis was also useful to analyze
350 low GEM concentrations, which were mainly linked to southerly polar air masses (Fig. S8), and
351 low Rn values, which were also traced to air masses traveling over the ocean from the Antarctic
352 (Fig. S8), which has low local emissions of Rn, being almost entirely covered by ice [72].

353 For each individual year, the analysis of 5-day backward trajectories reaching AMS revealed no
354 particular differences on both annual and seasonal scales (Fig. S9), although differences could be
355 expected on a seasonal basis at least for the summer of 2016 because of the occurrence of El Niño.

356 The four clusters of the 10-day backward trajectories resulting from the CA were clearly associated
357 with the marine environment, though coming from different sectors: The first cluster (C1)
358 collected a set of trajectories coming from N-NNE; the second (C2) and fourth (C4) clusters those

359 coming from the SW, probably intercepting masses also from the subantarctic and Antarctic
360 region, while the third (C3) from the NW sector collected trajectories probably intercepting masses
361 near the African continent (Fig. S10). These results allowed us to demonstrate that air masses
362 reaching AMS essentially traveled over the ocean, so we could assume that the origin of Hg was
363 related to the marine environment with occasional continental sources. This outcome agrees with
364 the literature on pollutant load at this site, which reports oceanic emissions and biomass burning
365 as the pathways that primarily influence the occurrence of pollution events.

366 The results of the CA were combined with the maps obtained from the PSCF technique for GEM
367 and Rn-222, thus obtaining indications about the most likely source location of these two
368 pollutants. The map obtained for GEM over the entire 2013-2019 period showed that the highest
369 values of GEM were associated with clusters C1 and C3 (Fig. 5), thus supporting our hypothesis
370 that the main contribution to GEM concentration was the emission from the subtropical ocean,
371 which contributed to depositional fluxes, as expected for marine regions [10]. The second GEM
372 source was probably of continental origin, arising from WNW air masses that crossed through
373 some areas of southern Africa, meeting the assumption of the influence of long-range transport on
374 the pollution load on Amsterdam Island. The detailed study of the PSCF maps by season did not
375 show significant differences in the PSCF probability, except for C1 where the highest values of
376 this probability were found during summer and IS2, two periods with higher solar radiation and
377 temperature gradient in the air-water interface that favor the emission of elemental Hg from surface
378 water [73]. As for the lower GEM values, the PSCF confirmed the limited contribution that
379 southerly polar air masses (C4 and C2 clusters) provided to the GEM concentration at AMS. In
380 summary, our findings suggested GEM levels on Amsterdam Island are consistent with primary
381 control by evasion from subtropical marine waters and transport from the African continent.
382 Besides, considering the lack of upward/downward trend in both GEM and VWMC, we can
383 surmise that there has been no evolution in the Hg emissions intercepted at AMS from Africa.

384 A different situation was found with Rn, for which the PSCF map in the entire period showed a
385 higher probability associated with cluster C3 (Fig. S11), also providing further evidence that the
386 cluster C3 was associated with trajectories coming from southern Africa. In addition, observation
387 of the seasonal PSCF maps clarified that Rn sourced most probably from the African inland in
388 winter and was transported to AMS (Fig. S11). In support of this conclusion, previous studies of
389 air mass backward trajectories ending at AMS and Rn measurements showed that southern Africa
390 (including Madagascar) was the predominant non-marine source of trace materials transported to
391 AMS [27,74,75].

392 **4. Conclusions**

393 Given the importance of Hg pollution control on a global scale, continuous measurements have
394 been carried out at the station on Amsterdam Island, a unique monitoring site in the Indian Ocean.
395 The GEM concentration throughout 2013-2019 was quite stationary, ranging from 0.70 to 1.58 ng
396 m⁻³, with an average value of 1.06 ± 0.07 ng m⁻³, following the typical background concentrations
397 in the Southern Hemisphere. The highest values were recorded during winter, presumably due to
398 the ITCZ variability that caused higher wind speed over the surface ocean, and the long-range
399 contribution of biomass burning from South Africa. In addition, the occurrence of the El Niño in
400 2016 led to GEM peaks which were detected at AMS with a delay of 6-8 months.

401 Statistical tools such as CA and PSCF showed that oceanic emission was the major driver of GEM,
402 while Rn-222 at AMS was primarily associated with long-range transport from southern Africa.
403 In precipitation, the VWMC of THg was 2.39 ± 1.17 ng L⁻¹ on average and varied between 1.16
404 and 4.67 ng L⁻¹, which corresponded to wet deposition fluxes between 1.06 and 3.31 $\mu\text{g m}^{-2} \text{yr}^{-1}$.
405 However, the substantial lack of increasing/decreasing trend for both GEM and VWMC suggested
406 that there was no clear evolution about emission of Hg transported to AMS from Africa, hence
407 numerous efforts still need to be made for an effective long-term reduction of the concentration of
408 this pollutant to fulfill the objectives of the MCM.

409 **Data availability:** AMS L2 GEM data (<https://doi.org/10.25326/168>) are freely available [37] at
410 <https://gmos.aeris-data.fr/> from a GMOS-FR data portal coordinated by IGE (Institut des
411 Géosciences de l'Environnement, Grenoble, France; technical PI: Olivier Magand) with the
412 support of the French national AERIS-SEDOO partners, data and services center for the
413 atmosphere (last access: 31 January 2022).

414 **Acknowledgments:** We deeply thank all overwintering staff at AMS and the French Polar
415 Institute Paul-Emile Victor (IPEV) staff and scientists who helped with the setup and maintenance
416 of the experiment at AMS in the framework of the GMOSTral-1028 IPEV program. AMS GEM
417 data were collected via instruments coordinated by the IGE-PTICHA technical platform dedicated
418 to atmospheric chemistry field instrumentation. The authors acknowledge the AERIS data
419 infrastructure for providing access to the GEM data in this study.

420 We thank Dr. Gianluca Bevacqua from the Language Centre of the University of Calabria and
421 CNR-IIA for the English proofreading of the manuscript.

422 **Funding:**

423 The authors from CNR-IIA would like to acknowledge the contribution received from the
424 following projects:

- 425 ■ FET Proactive project "Towards new frontiers for distributed environmental monitoring based on
426 an ecosystem of plant seed-like soft robots" (I-Seed). This project has received funding from the
427 European Union's Horizon 2020 research and innovation programme under grant agreement No
428 101017940.
- 429 ■ EMPIR - EURAMET project "Metrology for traceable protocols for elemental and oxidised
430 mercury concentrations" (SI-Hg); grant no. 19NRM03. This project (SI-Hg) has received funding
431 from the EMPIR programme co-financed by the Participating States and from the European
432 Union's Horizon 2020 research and innovation programme.
- 433 ■ Amsterdam Island GEM data, accessible in GMOS-FR national database ([https://gmos.aeris-
data.fr/](https://gmos.aeris-
434 data.fr/)) have been collected with funding from European Union 7th Framework Programme

435 project Global Mercury Observation System (GMOS 2010-2015), the French Polar Institute IPEV
436 via GMOSTral-1028 IPEV program since 2012, the LEFE CHAT CNRS/INSU (TOPMMODEL
437 program) and the H2020 ERA-PLANET (689443) iGOSP programme.

438 Author contribution statement:

439

440 Antonella Tassone; Olivier Magand: Conceived and designed the experiments; Performed the
441 experiments; Analyzed and interpreted the data; Contributed reagents, materials, analysis tools or
442 data; Wrote the paper. </p>

443

444 Attilio Naccarato: Conceived and designed the experiments; Analyzed and interpreted the data;
445 Contributed reagents, materials, analysis tools or data; Wrote the paper. </p>

446

447 Maria Martino; Domenico Amico; Hippolyte Leuridan; Michel Ramonet; Aurelien Dommergue:
448 Performed the experiments; Analyzed and interpreted the data; Contributed reagents, materials,
449 analysis tools or data; Wrote the paper. </p>

450

451 Francesca Sprovieri; Nicola Pirrone: Contributed reagents, materials, analysis tools or data; Wrote
452 the paper. </p>

453

454 Yann Bertrand: Performed the experiments; Contributed reagents, materials, analysis tools or data;
455 Wrote the paper. </p>

456

457 Funding statement:

458

459 Nicola Pirrone was supported by Horizon 2020 [101017940 and 19NRM03].

460

461 Data availability statement:

462

463 Data associated with this study has been deposited at <https://gmos.aeris-data.fr/>.

464

465 Declaration of interest's statement:

466

467 The authors declare no conflict of interest.

468

469 Additional information:

470

471 Supplementary content related to this article has been published online at [URL].

472

473

474

Journal Pre-proof

475 **References**

- 476 [1] H. Zhang, S. Wu, E.M. Leibensperger, Source-receptor relationships for atmospheric
477 mercury deposition in the context of global change, *Atmos. Environ.* 254 (2021) 118349.
478 <https://doi.org/10.1016/j.atmosenv.2021.118349>.
- 479 [2] F. Ciani, V. Rimondi, P. Costagliola, Atmospheric mercury pollution: the current
480 methodological framework outlined by environmental legislation, *Air Qual. Atmos. Heal.* 14
481 (2021) 1633–1645. <https://doi.org/10.1007/s11869-021-01044-4>.
- 482 [3] UNEP, Global Mercury Assessment 2018 | UNEP - UN Environment Programme, (2018).
483 <https://www.unep.org/resources/publication/global-mercury-assessment-2018> (accessed
484 April 19, 2021).
- 485 [4] UNEP, Minamata Convention on Mercury - Text and Annexes, UNEP, 2013a. (2013) 69.
- 486 [5] H. Selin, S.E. Keane, S. Wang, N.E. Selin, K. Davis, D. Bally, Linking science and policy to
487 support the implementation of the Minamata Convention on Mercury, *Ambio.* 47 (2018)
488 198–215. <https://doi.org/10.1007/s13280-017-1003-x>.
- 489 [6] D. Amico, A. Tassone, N. Pirrone, F. Sprovieri, A. Naccarato, Recent applications and novel
490 strategies for mercury determination in environmental samples using microextraction-based
491 approaches: A review, *J. Hazard. Mater.* 433 (2022) 128823.
492 <https://doi.org/10.1016/j.jhazmat.2022.128823>.
- 493 [7] A. Naccarato, A. Tassone, F. Cavaliere, R. Elliani, N. Pirrone, F. Sprovieri, A. Tagarelli, A.
494 Giglio, Agrochemical treatments as a source of heavy metals and rare earth elements in
495 agricultural soils and bioaccumulation in ground beetles, *Sci. Total Environ.* 749 (2020)
496 141438. <https://doi.org/10.1016/j.scitotenv.2020.141438>.
- 497 [8] A. Naccarato, A. Tassone, M. Martino, R. Elliani, F. Sprovieri, N. Pirrone, A. Tagarelli, An
498 innovative green protocol for the quantification of benzothiazoles, benzotriazoles and
499 benzosulfonamides in PM10 using microwave-assisted extraction coupled with solid-phase
500 microextraction gas chromatography tandem-mass spectrometry, *Environ. Pollut.* 285 (2021)

- 501 117487. <https://doi.org/10.1016/j.envpol.2021.117487>.
- 502 [9] A. Naccarato, A. Tassone, M. Martino, S. Moretti, A. Macagnano, E. Zampetti, P. Papa, J.
503 Avossa, N. Pirrone, M. Nerentorp, J. Munthe, I. Wängberg, G.W. Stuppel, C.P.J.J. Mitchell,
504 A.R. Martin, A. Steffen, D. Babi, E.M. Prestbo, F. Sprovieri, F. Wania, A field
505 intercomparison of three passive air samplers for gaseous mercury in ambient air, *Atmos.*
506 *Meas. Tech.* 14 (2021) 3657–3672. <https://doi.org/10.5194/amt-14-3657-2021>.
- 507 [10] F. Sprovieri, N. Pirrone, M. Bencardino, F. D'Amore, H. Angot, C. Barbante, E.-G. Brunke,
508 F. Arcega-Cabrera, W. Cairns, S. Comero, M. del C. Diéguez, A. Dommergue, R.
509 Ebinghaus, X. Bin Feng, X. Fu, P.E. Garcia, B.M. Gawlik, U. Hageström, K. Hansson, M.
510 Horvat, J. Kotnik, C. Labuschagne, O. Magand, L. Martin, N. Mashyanov, T. Mkololo, J.
511 Munthe, V. Obolkin, M. Ramirez Islas, F. Sena, V. Somerset, P. Spandow, M. Vardè, C.
512 Walters, I. Wängberg, A. Weigelt, X. Yang, H. Zhang, Five-year records of mercury wet
513 deposition flux at GMOS sites in the Northern and Southern hemispheres, *Atmos. Chem.*
514 *Phys.* 17 (2017) 2689–2708. <https://doi.org/10.5194/acp-17-2689-2017>.
- 515 [11] F. Sprovieri, N. Pirrone, M. Bencardino, F. D'Amore, F. Carbone, S. Cinnirella, V.
516 Mannarino, M. Landis, R. Ebinghaus, A. Weigelt, E.G. Brunke, C. Labuschagne, L. Martin,
517 J. Munthe, I. Wängberg, P. Artaxo, F. Morais, H. De Melo Jorge Barbosa, J. Brito, W.
518 Cairns, C. Barbante, M. Del Carmen Diéguez, P. Elizabeth Garcia, D. Aurélien, H. Angot, O.
519 Magand, H. Skov, M. Horvat, J. Kotnik, K. Alana Read, L. Mendes Neves, B. Manfred
520 Gawlik, F. Sena, N. Mashyanov, V. Obolkin, D. Wip, X. Bin Feng, H. Zhang, X. Fu, R.
521 Ramachandran, D. Cossa, J. Knoery, N. Maruszczak, M. Nerentorp, C. Norstrom,
522 Atmospheric mercury concentrations observed at ground-based monitoring sites globally
523 distributed in the framework of the GMOS network, *Atmos. Chem. Phys.* 16 (2016) 11915–
524 11935. <https://doi.org/10.5194/acp-16-11915-2016>.
- 525 [12] G.-R. Sheu, N.-H. Lin, Characterizations of wet mercury deposition to a remote islet
526 (Pengjiayu) in the subtropical Northwest Pacific Ocean, *Atmos. Environ.* 77 (2013) 474–481.

- 527 <https://doi.org/10.1016/j.atmosenv.2013.05.038>.
- 528 [13] Sheu, Gay, Schmeltz, Olson, Chang, Lin, Nguyen, A New Monitoring Effort for Asia: The
529 Asia Pacific Mercury Monitoring Network (APMMN), *Atmosphere (Basel)*. 10 (2019) 481.
530 <https://doi.org/10.3390/atmos10090481>.
- 531 [14] K.A. Pfaffhuber, T. Berg, D. Hirdman, A. Stohl, Atmospheric mercury observations from
532 Antarctica: seasonal variation and source and sink region calculations, *Atmos. Chem. Phys.*
533 12 (2012) 3241–3251. <https://doi.org/10.5194/acp-12-3241-2012>.
- 534 [15] F. Slemr, H. Angot, A. Dommergue, O. Magand, M. Barret, A. Weigelt, R. Ebinghaus, E.G.
535 Brunke, K.A. Pfaffhuber, G. Edwards, D. Howard, J. Powell, M. Keywood, F. Wang,
536 Comparison of mercury concentrations measured at several sites in the Southern Hemisphere,
537 *Atmos. Chem. Phys.* 15 (2015) 3125–3133. <https://doi.org/10.5194/acp-15-3125-2015>.
- 538 [16] F. Slemr, L. Martin, C. Labuschagne, T. Mkololo, H. Angot, O. Magand, A. Dommergue, P.
539 Garat, M. Ramonet, J. Bieser, Atmospheric mercury in the Southern Hemisphere – Part 1:
540 Trend and inter-annual variations in atmospheric mercury at Cape Point, South Africa, in
541 2007–2017, and on Amsterdam Island in 2012–2017, *Atmos. Chem. Phys.* 20 (2020) 7683–
542 7692. <https://doi.org/10.5194/acp-20-7683-2020>.
- 543 [17] H. Angot, M. Barret, O. Magand, M. Ramonet, A. Dommergue, A 2-year record of
544 atmospheric mercury species at a background Southern Hemisphere station on Amsterdam
545 Island, *Atmos. Chem. Phys.* 14 (2014) 11461–11473. [https://doi.org/10.5194/acp-14-11461-](https://doi.org/10.5194/acp-14-11461-2014)
546 2014.
- 547 [18] H. Angot, A. Dastoor, F. De Simone, K. Gärdfeldt, C.N. Gencarelli, I.M. Hedgecock, S.
548 Langer, O. Magand, M.N. Mastromonaco, C. Nordstrøm, K.A. Pfaffhuber, N. Pirrone, A.
549 Ryjkov, N.E. Selin, H. Skov, S. Song, F. Sprovieri, A. Steffen, K. Toyota, O. Travnikov, X.
550 Yang, A. Dommergue, Chemical cycling and deposition of atmospheric mercury in polar
551 regions: Review of recent measurements and comparison with models, *Atmos. Chem. Phys.*
552 16 (2016) 10735–10763. <https://doi.org/10.5194/ACP-16-10735-2016>.

- 553 [19] H. Angot, I. Dion, N. Vogel, M. Legrand, O. Magand, A. Dommergue, Multi-year record of
554 atmospheric mercury at Dumont d'Urville, East Antarctic coast: Continental outflow and
555 oceanic influences, *Atmos. Chem. Phys.* 16 (2016) 8265–8279. [https://doi.org/10.5194/ACP-](https://doi.org/10.5194/ACP-16-8265-2016)
556 16-8265-2016.
- 557 [20] E.-G. Brunke, C. Walters, T. Mkololo, L. Martin, C. Labuschagne, B. Silwana, F. Slemr, A.
558 Weigelt, R. Ebinghaus, V. Somerset, Mercury in the atmosphere and in rainwater at Cape
559 Point, South Africa, *Atmos. Environ.* 125 (2016) 24–32.
560 <https://doi.org/10.1016/j.atmosenv.2015.10.059>.
- 561 [21] E.-G. Brunke, R. Ebinghaus, H.H. Kock, C. Labuschagne, F. Slemr, Emissions of mercury in
562 southern Africa derived from long-term observations at Cape Point, South Africa, *Atmos.*
563 *Chem. Phys.* 12 (2012) 7465–7474. <https://doi.org/10.5194/acp-12-7465-2012>.
- 564 [22] M.C. Diéguez, M. Bencardino, P.E. García, F. D'Amore, J. Castagna, F. De Simone, C. Soto
565 Cárdenas, S. Ribeiro Guevara, N. Pirrone, F. Sprovieri, A multi-year record of atmospheric
566 mercury species at a background mountain station in Andean Patagonia (Argentina):
567 Temporal trends and meteorological influence, *Atmos. Environ.* 214 (2019) 116819.
568 <https://doi.org/10.1016/j.atmosenv.2019.116819>.
- 569 [23] A.M. Koenig, O. Magand, P. Laj, M. Andrade, I. Moreno, F. Velarde, G. Salvatierra, R.
570 Gutierrez, L. Blacutt, D. Aliaga, T. Reichler, K. Sellegri, O. Laurent, M. Ramonet, A.
571 Dommergue, Seasonal patterns of atmospheric mercury in tropical South America as inferred
572 by a continuous total gaseous mercury record at Chacaltaya station (5240 m) in Bolivia,
573 *Atmos. Chem. Phys.* 21 (2021) 3447–3472. <https://doi.org/10.5194/acp-21-3447-2021>.
- 574 [24] M. Martino, A. Tassone, L. Angiuli, A. Naccarato, P.R. Dambruoso, F. Mazzone, L. Trizio,
575 C. Leonardi, F. Petracchini, F. Sprovieri, N. Pirrone, F. D'Amore, M. Bencardino, First
576 atmospheric mercury measurements at a coastal site in the Apulia region: seasonal variability
577 and source analysis, *Environ. Sci. Pollut. Res.* (2022) 16. [https://doi.org/10.1007/s11356-](https://doi.org/10.1007/s11356-022-20505-6)
578 022-20505-6.

- 579 [25] J. Bieser, H. Angot, F. Slemr, L. Martin, Atmospheric mercury in the Southern Hemisphere –
580 Part 2: Source apportionment analysis at Cape Point station, South Africa, *Atmos. Chem.*
581 *Phys.* 20 (2020) 10427–10439. <https://doi.org/10.5194/acp-20-10427-2020>.
- 582 [26] A. Gaudry, P. Monfray, G. Polian, G. Bonsang, B. Ardouin, A. Jegou, G. Lambert, Non-
583 seasonal variations of atmospheric CO₂ concentrations at Amsterdam Island, *Tellus B*
584 *Chem. Phys. Meteorol.* 43 (1991) 136–143. <https://doi.org/10.3402/tellusb.v43i2.15258>.
- 585 [27] V. Gros, B. Bonsang, D. Martin, P.C. Novelli, V. Kazan, Carbon monoxide short term
586 measurements at Amsterdam island: estimations of biomass burning emission rates,
587 *Chemosph. - Glob. Chang. Sci.* 1 (1999) 163–172. [https://doi.org/10.1016/S1465-](https://doi.org/10.1016/S1465-9972(99)00009-4)
588 [9972\(99\)00009-4](https://doi.org/10.1016/S1465-9972(99)00009-4).
- 589 [28] V. Gros, B. Bonsang, R. Sarda Esteve, Atmospheric carbon monoxide ‘in situ’ monitoring by
590 automatic gas chromatography, *Chemosph. - Glob. Chang. Sci.* 1 (1999) 153–161.
591 [https://doi.org/10.1016/S1465-9972\(99\)00010-0](https://doi.org/10.1016/S1465-9972(99)00010-0).
- 592 [29] M. Jiskra, J.E. Sonke, D. Obrist, J. Bieser, R. Ebinghaus, C.L. Myhre, K.A. Pfaffhuber, I.
593 Wängberg, K. Kyllönen, D. Worthy, L.G. Martin, C. Labuschagne, T. Mkololo, M. Ramonet,
594 O. Magand, A. Dommergue, A vegetation control on seasonal variations in global
595 atmospheric mercury concentrations, *Nat. Geosci.* 11 (2018) 244–250.
596 <https://doi.org/10.1038/s41561-018-0078-8>.
- 597 [30] C. Yver-Kwok, C. Philippon, P. Bergamaschi, T. Biermann, F. Calzolari, H. Chen, S. Conil,
598 P. Cristofanelli, M. Delmotte, J. Hatakka, M. Heliasz, O. Hermansen, K. Kominkova, D.
599 Kubistin, N. Kumps, O. Laurent, T. Laurila, I. Lehner, J. Levula, M. Lindauer, M. Lopez, I.
600 Mammarella, G. Manca, P. Marklund, J.M. Metzger, M. Mölder, S.M. Platt, M. Ramonet, L.
601 Rivier, B. Scheeren, M. Kumar Sha, P. Smith, M. Steinbacher, G. Vítková, S. Wyss,
602 Evaluation and optimization of ICOS atmosphere station data as part of the labeling process,
603 *Atmos. Meas. Tech.* 14 (2021) 89–116. <https://doi.org/10.5194/AMT-14-89-2021>.
- 604 [31] S.D. Chambers, S. Preunkert, R. Weller, S.-B. Hong, R.S. Humphries, L. Tositti, H. Angot,

- 605 M. Legrand, A.G. Williams, A.D. Griffiths, J. Crawford, J. Simmons, T.J. Choi, P.B.
606 Krummel, S. Molloy, Z. Loh, I. Galbally, S. Wilson, O. Magand, F. Sprovieri, N. Pirrone, A.
607 Dommergue, Characterizing Atmospheric Transport Pathways to Antarctica and the Remote
608 Southern Ocean Using Radon-222, *Front. Earth Sci.* 6 (2018) 1–28.
609 <https://doi.org/10.3389/feart.2018.00190>.
- 610 [32] A. Gaudry, G. Polian, B. Ardouin, G. Lambert, Radon-calibrated emissions of CO₂ from
611 South Africa, *Tellus B Chem. Phys. Meteorol.* 42 (1990) 9–19.
612 <https://doi.org/10.3402/tellusb.v42i1.15187>.
- 613 [33] L. Harrison, C. Funk, A. McNally, S. Shukla, G. Husak, Pacific sea surface temperature
614 linkages with Tanzania’s multi-season drying trends, *Int. J. Climatol.* 39 (2019) 3057–3075.
615 <https://doi.org/10.1002/joc.6003>.
- 616 [34] F. D’Amore, M. Bencardino, S. Cinnirella, F. Sprovieri, N. Pirrone, Data quality through a
617 web-based QA/QC system: Implementation for atmospheric mercury data from the global
618 mercury observation system, *Environ. Sci. Process. Impacts.* 17 (2015) 1482–1491.
619 <https://doi.org/10.1039/c5em00205b>.
- 620 [35] A. Tassone, S. Moretti, M. Martino, N. Pirrone, F. Sprovieri, A. Naccarato, Modification of
621 the EPA method 1631E for the quantification of total mercury in natural waters, *MethodsX.* 7
622 (2020) 100987. <https://doi.org/10.1016/j.mex.2020.100987>.
- 623 [36] GMOS, Method for the determination of total mercury in precipitation, *GMOS.* (2011) 1–22.
- 624 [37] O. Magand, A. Dommergue, Continuous measurements of atmospheric mercury at
625 Amsterdam Island (L2) [Dataset]. *Aeris.*, (2021).
626 <https://doi.org/https://doi.org/10.25326/168>.
- 627 [38] P.K. Sen, Estimates of the Regression Coefficient Based on Kendall’s Tau, *J. Am. Stat.*
628 *Assoc.* 63 (1968) 1379. <https://doi.org/10.2307/2285891>.
- 629 [39] M.J. McGill, R.J. Swap, J.E. Yorks, P.A. Selmer, S.J. Piketh, Observation and quantification
630 of aerosol outflow from southern Africa using spaceborne lidar, *S. Afr. J. Sci.* 116 (2020)

- 631 65–70. <https://doi.org/10.17159/sajs.2020/6398>.
- 632 [40] E. Baboukas, J. Sciare, N. Mihalopoulos, Spatial, Temporal and Interannual Variability of
633 Methanesulfonate and Non-Sea-Salt Sulfate in Rainwater in the Southern Indian Ocean
634 (Amsterdam, Crozet and Kerguelen Islands), *J. Atmos. Chem.* 48 (2004) 35–57.
635 <https://doi.org/10.1023/B:JOCH.0000034508.13326.cd>.
- 636 [41] R.R. Draxler, G.D. Rolph, HYSPLIT (HYbrid Single-Particle Lagrangian Integrated
637 Trajectory), NOAA Air Resour. Lab. Coll. Park. MD. (2003).
638 <http://www.arl.noaa.gov/ready/hysplit4.html> (accessed May 3, 2022).
- 639 [42] J.L. Moody, P.J. Samson, The influence of atmospheric transport on precipitation chemistry
640 at two sites in the midwestern United States, *Atmos. Environ.* 23 (1989) 2117–2132.
641 [https://doi.org/10.1016/0004-6981\(89\)90173-X](https://doi.org/10.1016/0004-6981(89)90173-X).
- 642 [43] J.H. Ward, Hierarchical Grouping to optimize an objective function, *J. Am. Stat. Assoc.* 58
643 (1963) 236–244.
- 644 [44] M.S. Landis, G.J. Keeler, Atmospheric mercury deposition to Lake Michigan during the
645 Lake Michigan Mass Balance Study, *Environ. Sci. Technol.* (2002).
646 <https://doi.org/10.1021/es011217b>.
- 647 [45] D.S. Wilks, *Statistical Methods in the Atmospheric Sciences*, Fourth, Elsevier, Oxford, 2019.
648 <https://doi.org/10.1016/C2017-0-03921-6>.
- 649 [46] M. Anjos, A.C. Targino, P. Krecl, G.Y. Oukawa, R.F. Braga, Analysis of the urban heat
650 island under different synoptic patterns using local climate zones, *Build. Environ.* 185 (2020)
651 107268. <https://doi.org/10.1016/J.BUILDENV.2020.107268>.
- 652 [47] R.R. Draxler, HYSPLIT4 User 's Guide, Silver Spring, USA, 1999.
653 <http://www.arl.noaa.gov/hysplit.html>.
- 654 [48] Z.L. Fleming, P.S. Monks, A.J. Manning, Review: Untangling the influence of air-mass
655 history in interpreting observed atmospheric composition, *Atmos. Res.* (2012).
- 656 [49] N. Pekney, C. Davidson, L. Zhou, P. Hopke, Application of PSCF and CPF to PMF-modeled

- 657 sources of PM_{2.5} in Pittsburgh, in: *Aerosol Sci. Technol.*, 2006: pp. 952–961.
658 <https://doi.org/10.1080/02786820500543324>.
- 659 [50] K.R. Travis, C.L. Heald, H.M. Allen, E.C. Apel, S.R. Arnold, D.R. Blake, W.H. Brune, X.
660 Chen, R. Commane, J.D. Crouse, B.C. Daube, G.S. Diskin, J.W. Elkins, M.J. Evans, S.R.
661 Hall, E.J. Hints, R.S. Hornbrook, P.S. Kasibhatla, M.J. Kim, G. Luo, K. McKain, D.B.
662 Millet, F.L. Moore, J. Peischl, T.B. Ryerson, T. Sherwen, A.B. Thames, K. Ullmann, X.
663 Wang, P.O. Wennberg, G.M. Wolfe, F. Yu, Constraining remote oxidation capacity with
664 ATom observations, *Atmos. Chem. Phys.* 20 (2020) 7753–7781. [https://doi.org/10.5194/acp-](https://doi.org/10.5194/acp-20-7753-2020)
665 [20-7753-2020](https://doi.org/10.5194/acp-20-7753-2020).
- 666 [51] D.P. Edwards, L.K. Emmons, J.C. Gille, A. Chu, J.L. Attié, L. Giglio, S.W. Wood, J.
667 Haywood, M.N. Deeter, S.T. Massie, D.C. Ziskin, J.R. Drummond, Satellite-observed
668 pollution from Southern Hemisphere biomass burning, *J. Geophys. Res. Atmos.* 111 (2006)
669 1–17. <https://doi.org/10.1029/2005JD006655>.
- 670 [52] M.A.K. Khalil, R.A. Rasmussen, Sources, sinks, and seasonal cycles of atmospheric
671 methane, *J. Geophys. Res. Ocean.* 88 (1983) 5131–5144.
672 <https://doi.org/10.1029/JC088iC09p05131>.
- 673 [53] M.A.K. Khalil, R.A. Rasmussen, The global cycle of carbon monoxide: Trends and mass
674 balance, *Chemosphere.* 20 (1990) 227–242. [https://doi.org/10.1016/0045-6535\(90\)90098-E](https://doi.org/10.1016/0045-6535(90)90098-E).
- 675 [54] J. Williams, V. Gros, B. Bonsang, V. Kazan, HO cycle in 1997 and 1998 over the southern
676 Indian Ocean derived from CO, radon, and hydrocarbon measurements made at Amsterdam
677 Island, *J. Geophys. Res. Atmos.* 106 (2001) 12719–12725.
678 <https://doi.org/10.1029/2001JD900116>.
- 679 [55] E.-G. Brunke, C. Labuschagne, B. Parker, H.E. Scheel, S. Whittlestone, Baseline air mass
680 selection at Cape Point, South Africa: application of 222Rn and other filter criteria to CO₂,
681 *Atmos. Environ.* 38 (2004) 5693–5702. <https://doi.org/10.1016/j.atmosenv.2004.04.024>.
- 682 [56] D.S. McLagan, C.P.J. Mitchell, A. Steffen, H. Hung, C. Shin, G.W. Stupple, M.L. Olson,

- 683 W.T. Luke, P. Kelley, D. Howard, G.C. Edwards, P.F. Nelson, H. Xiao, G.R. Sheu, A.
684 Dreyer, H. Huang, B. Abdul Hussain, Y.D. Lei, I. Tavshunsky, F. Wania, Global evaluation
685 and calibration of a passive air sampler for gaseous mercury, *Atmos. Chem. Phys.* 18 (2018)
686 5905–5919. <https://doi.org/10.5194/acp-18-5905-2018>.
- 687 [57] J.A. Fisher, P.F. Nelson, Atmospheric mercury in Australia, *Elem. Sci. Anthr.* 8 (2020) 1–20.
688 <https://doi.org/10.1525/elementa.2020.070>.
- 689 [58] C. Liu, X. Liao, J. Qiu, Y. Yang, X. Feng, R.P. Allan, N. Cao, J. Long, J. Xu, Observed
690 variability of intertropical convergence zone over 1998-2018, *Environ. Res. Lett.* 15 (2020).
691 <https://doi.org/10.1088/1748-9326/aba033>.
- 692 [59] H. Lashkari, M. Jafari, Annual displacement and appropriate index to determine ITCZ
693 position in East Africa and the Indian Ocean regions, *Meteorol. Atmos. Phys.* 133 (2021)
694 1111–1126. <https://doi.org/10.1007/s00703-021-00797-y>.
- 695 [60] G. Liu, Y. Cai, N. O’Driscoll, *Environmental Chemistry and Toxicology of Mercury*, 2011.
696 <https://doi.org/10.1002/9781118146644>.
- 697 [61] Y.-S. Seo, Y.-J. Han, H.-D. Choi, T.M. Holsen, S.-M. Yi, Characteristics of total mercury
698 (TM) wet deposition: Scavenging of atmospheric mercury species, *Atmos. Environ.* 49
699 (2012) 69–76. <https://doi.org/10.1016/j.atmosenv.2011.12.031>.
- 700 [62] X. Fu, X. Yang, X. Lang, J. Zhou, H. Zhang, B. Yu, H. Yan, C.J. Lin, X. Feng, Atmospheric
701 wet and litterfall mercury deposition at urban and rural sites in China, *Atmos. Chem. Phys.*
702 16 (2016) 11547–11562. <https://doi.org/10.5194/acp-16-11547-2016>.
- 703 [63] V. Shah, D.J. Jacob, C.P. Thackray, X. Wang, E.M. Sunderland, T.S. Dibble, A. Saiz-Lopez,
704 I. Cernusák, V. Kellö, P.J. Castro, R. Wu, C. Wang, Improved mechanistic model of the
705 atmospheric redox chemistry of mercury, *Environ. Sci. Technol.* 55 (2021) 14445–14456.
706 <https://doi.org/10.1021/acs.est.1c03160>.
- 707 [64] H.M. Horowitz, D.J. Jacob, Y. Zhang, T.S. Dibble, F. Slemr, H.M. Amos, J.A. Schmidt, E.S.
708 Corbitt, E.A. Marais, E.M. Sunderland, A new mechanism for atmospheric mercury redox

- 709 chemistry: Implications for the global mercury budget, *Atmos. Chem. Phys.* 17 (2017) 6353–
710 6371. <https://doi.org/10.5194/acp-17-6353-2017>.
- 711 [65] O. Travníkov, H. Angot, P. Artaxo, M. Bencardino, J. Bieser, F. D'Amore, A. Dastoor, F. De
712 Simone, M.C. DIéguez, A. Dommergue, R. Ebinghaus, X. Bin Feng, C.N. Gencarelli, I.M.
713 Hedgecock, O. Magand, L. Martin, V. Matthias, N. Mashyanov, N. Pirrone, R.
714 Ramachandran, K. Alana Read, A. Ryjkov, N.E. Selin, F. Sena, S. Song, F. Sprovieri, D.
715 Wip, I. Wängberg, X. Yang, Multi-model study of mercury dispersion in the atmosphere:
716 Atmospheric processes and model evaluation, *Atmos. Chem. Phys.* 17 (2017) 5271–5295.
717 <https://doi.org/10.5194/acp-17-5271-2017>.
- 718 [66] R. V. Rohli, A.J. Vega, *Climatology*, Jones & Bartlett Learning, 2015.
- 719 [67] F. Slemr, C.A. Brenninkmeijer, A. Rauthe-Schöch, A. Weigelt, R. Ebinghaus, E. Brunke, L.
720 Martin, T.G. Spain, S. O'Doherty, El Niño–Southern Oscillation influence on tropospheric
721 mercury concentrations, *Geophys. Res. Lett.* 43 (2016) 1766–1771.
722 <https://doi.org/10.1002/2016GL067949>.
- 723 [68] R.A. Preston-Whyte, P.D. Tyson, *Atmosphere and weather of southern Africa*, Oxford
724 University Press, 1988. [https://agris.fao.org/agris-](https://agris.fao.org/agris-search/search.do?recordID=US201300685112)
725 [search/search.do?recordID=US201300685112](https://agris.fao.org/agris-search/search.do?recordID=US201300685112) (accessed November 19, 2021).
- 726 [69] F. Carbone, M.S. Landis, C.N. Gencarelli, A. Naccarato, F. Sprovieri, F. De Simone, I.M.
727 Hedgecock, N. Pirrone, Sea surface temperature variation linked to elemental mercury
728 concentrations measured on Mauna Loa, *Geophys. Res. Lett.* (2016).
729 <https://doi.org/10.1002/2016GL069252>.
- 730 [70] L.S.P. Nguyen, K.T. Nguyen, S.M. Griffith, G.R. Sheu, M.C. Yen, S.C. Chang, N.H. Lin,
731 Multiscale Temporal Variations of Atmospheric Mercury Distinguished by the Hilbert–
732 Huang Transform Analysis Reveals Multiple El Niño–Southern Oscillation Links, *Environ.*
733 *Sci. Technol.* 56 (2022) 1423–1432. <https://doi.org/10.1021/acs.est.1c03819>.
- 734 [71] S. Huang, Y. Zhang, Interannual Variability of Air-Sea Exchange of Mercury in the Global

- 735 Ocean: The “seesaw Effect” in the Equatorial Pacific and Contributions to the Atmosphere,
736 Environ. Sci. Technol. 55 (2021) 7145–7156. <https://doi.org/10.1021/acs.est.1c00691>.
- 737 [72] G. Polian, G. Lambert, B. Ardouin, A. Jegou, Long-range transport of continental radon in
738 subantarctic and antarctic areas, Tellus B Chem. Phys. Meteorol. 38 (1986) 178–189.
739 <https://doi.org/10.3402/tellusb.v38i3-4.15126>.
- 740 [73] C.. deW. Rautenbach, I.. Smith, Teleconnections between global sea-surface temperatures
741 and the interannual variability of observed and model simulated rainfall over southern Africa,
742 J. Hydrol. 254 (2001) 1–15. [https://doi.org/10.1016/S0022-1694\(01\)00454-1](https://doi.org/10.1016/S0022-1694(01)00454-1).
- 743 [74] J.M. Miller, J.L. Moody, J.M. Harris, A. Gaudry, A 10-year trajectory flow climatology for
744 Amsterdam Island, 1980–1989, Atmos. Environ. Part A. Gen. Top. 27 (1993) 1909–1916.
745 [https://doi.org/10.1016/0960-1686\(93\)90296-B](https://doi.org/10.1016/0960-1686(93)90296-B).
- 746 [75] M. Ramonet, J.C. Le Roulley, P. Bousquet, P. Monfray, Radon-222 Measurements During
747 the Tropoz II Campaign and Comparison With a Global Atmospheric Transport Model, J.
748 OfAtmospheric Chem. 23 (1996) 107–136.
- 749

750 **Figure captions**

751 **Fig. 1.** The plot of the seasonal volume-weighted mean concentration (VWMC) of total mercury
752 in rainwater and rainfall amount in the 2013-2019 period (IS1 = M-A-M-J; austral winter = J-A-
753 S; IS2 = O-N; austral summer = D-J-F).

754 **Fig. 2.** Temporal variability of Gaseous Elemental Mercury (GEM) from March 2013 to
755 December 2019: Individual hourly mean values (left panel) and monthly median values (right
756 panel). The shadings in the monthly median plot represent 25/75th and 5/95th quantile values.

757 **Fig. 3.** Correlation plots of seasonal averages of VWMC versus total rainfall (upper left); GEM
758 versus total rainfall (upper right); VWMC versus GEM (lower left); Wet deposition flux versus
759 rainfall (lower right).

760 **Fig. 4.** Temporal plot of the SOI, ONI, MEI indexes during the monitored period useful to assess
761 ENSO occurrence and trend of GEM over the same period. (For a better visualization, SOI was
762 sign-changed using multiplication by -1). The exceedance of the threshold of ± 0.5 °C of the ONI
763 for five consecutive months is used as evidence of El Niño (+0.5 °C), as well as large positive
764 values of -SOI and MEI. The light green box indicates the occurrence of the El Niño.

765 **Fig. 5.** The plot of the PSCF probabilities for GEM concentrations (90th percentile) at AMS in
766 the 2013-2019 period. The round black dot indicates the location of Amsterdam Island.

767

768

769 **Table 1.** Annual mean (\pm standard deviation) of the meteorological variables and monitored
 770 gases, namely CO₂, CO, Rn-222, CH₄, and Gaseous Elemental Mercury (GEM) at AMS from
 771 March 2013 to December 2019. Annual mean (\pm standard deviation) of volume-weighted mean
 772 concentration (VWMC) of total mercury in rainwater and wet deposition fluxes are also reported.
 773 (n.a.=not available)

774

	Temperature (°C)	Rainfall (mm)	CO ₂ (ppm)	CO (ppb)	Rn-222 (mBq m ⁻³)	CH ₄ (ppb)	GEM (ng m ⁻³)	VWMC (ng L ⁻¹)	Wet deposition flux ($\mu\text{g m}^{-2} \text{ year}^{-1}$)
2013	13.7 \pm 2.2	833	393.4 \pm 0.8	n.a.	48.1 \pm 19.4	1769 \pm 11	1.04 \pm 0.09	2.34 \pm 0.93	1.95 \pm 0.15
2014	14.2 \pm 2.8	864	395.2 \pm 0.9	n.a.	41.7 \pm 14.2	1774 \pm 15	1.05 \pm 0.06	1.80 \pm 1.07	1.55 \pm 0.33
2015	14.4 \pm 2.8	916	397.5 \pm 0.9	50.0 \pm 3.3	46.8 \pm 13.4	1786 \pm 14	1.02 \pm 0.07	1.16 \pm 0.30	1.06 \pm 0.13
2016	14.5 \pm 2.9	967	400.7 \pm 1.0	52.1 \pm 6.7	24.1 \pm 8.3	1792 \pm 12	1.08 \pm 0.06	3.04 \pm 1.39	2.94 \pm 0.44
2017	15.0 \pm 2.9	894	402.7 \pm 0.9	45.2 \pm 6.8	32.0 \pm 7.5	1799 \pm 15	1.02 \pm 0.08	2.18 \pm 1.63	1.95 \pm 0.31
2018	14.8 \pm 3.3	855	405.2 \pm 0.9	42.8 \pm 8.1	31.1 \pm 8.8	1810 \pm 14	1.08 \pm 0.05	4.67 \pm 3.95	3.31 \pm 0.58
2019	14.3 \pm 3.0	1003	407.6 \pm 1.1	50.5 \pm 7.8	26.9 \pm 7.1	1817 \pm 13	1.08 \pm 0.06	1.55 \pm 0.47	1.55 \pm 0.26

2013

2014

2015

2016

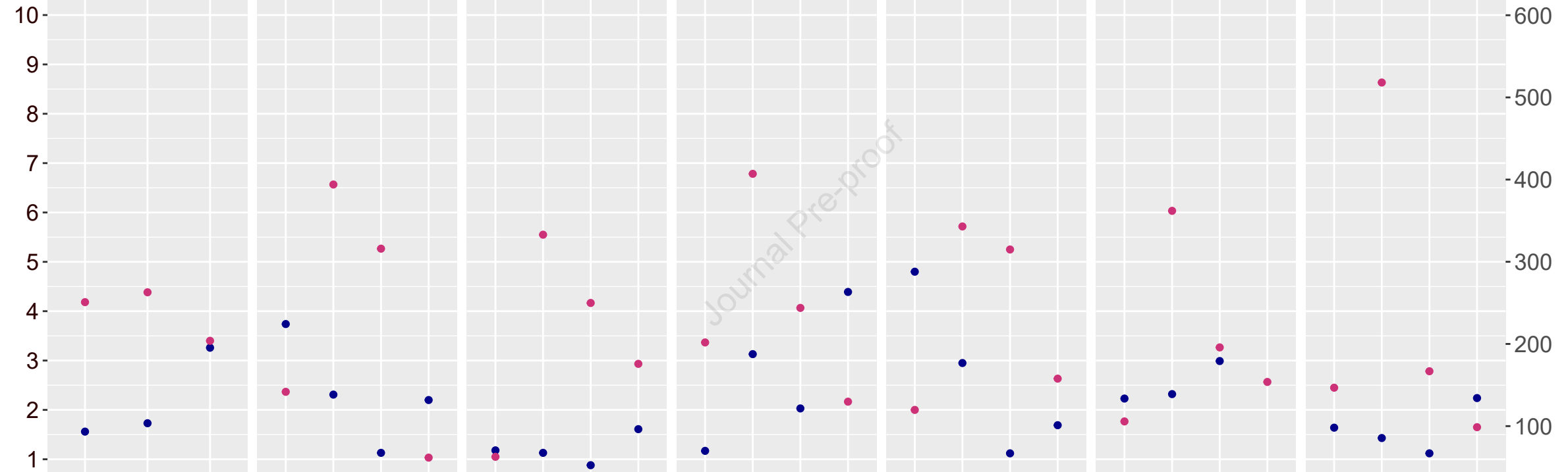
2017

2018

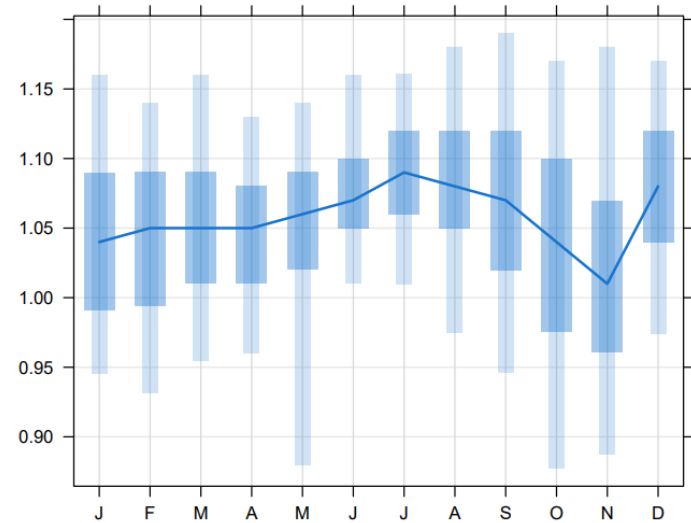
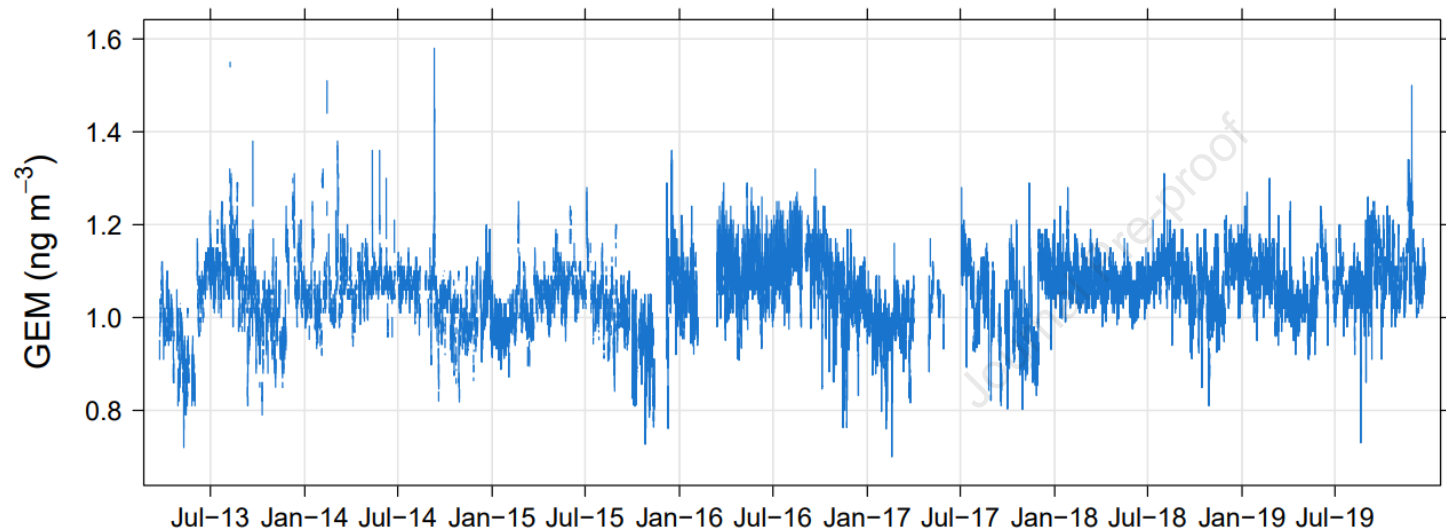
2019

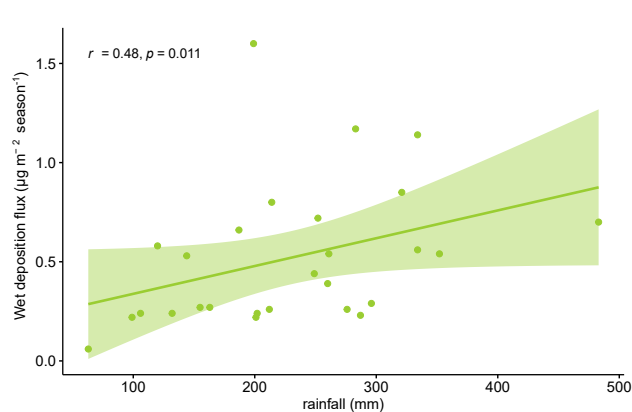
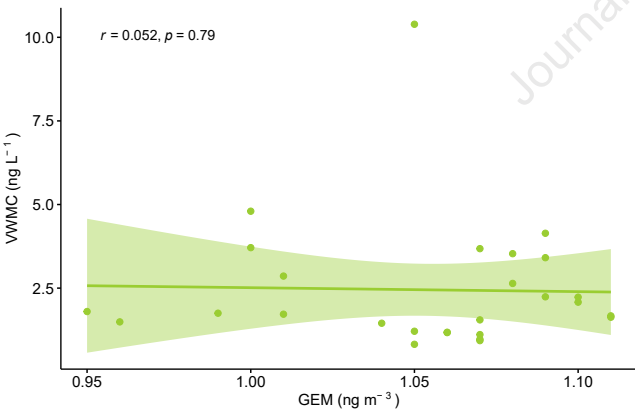
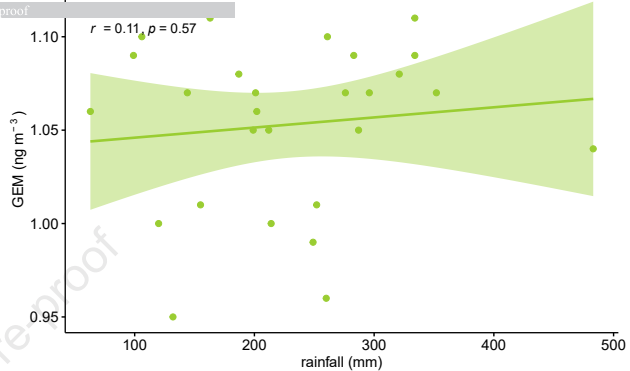
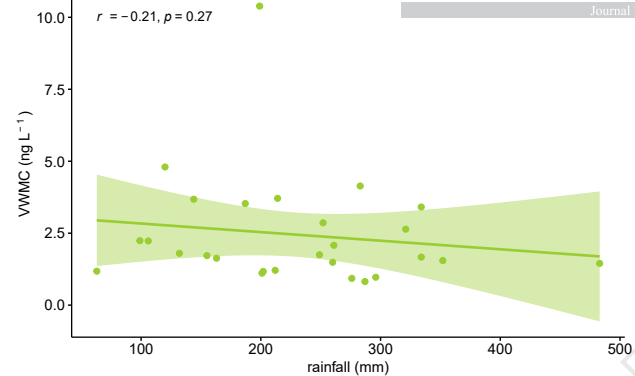
VWMC (ng L⁻¹)

rainfall (mm)

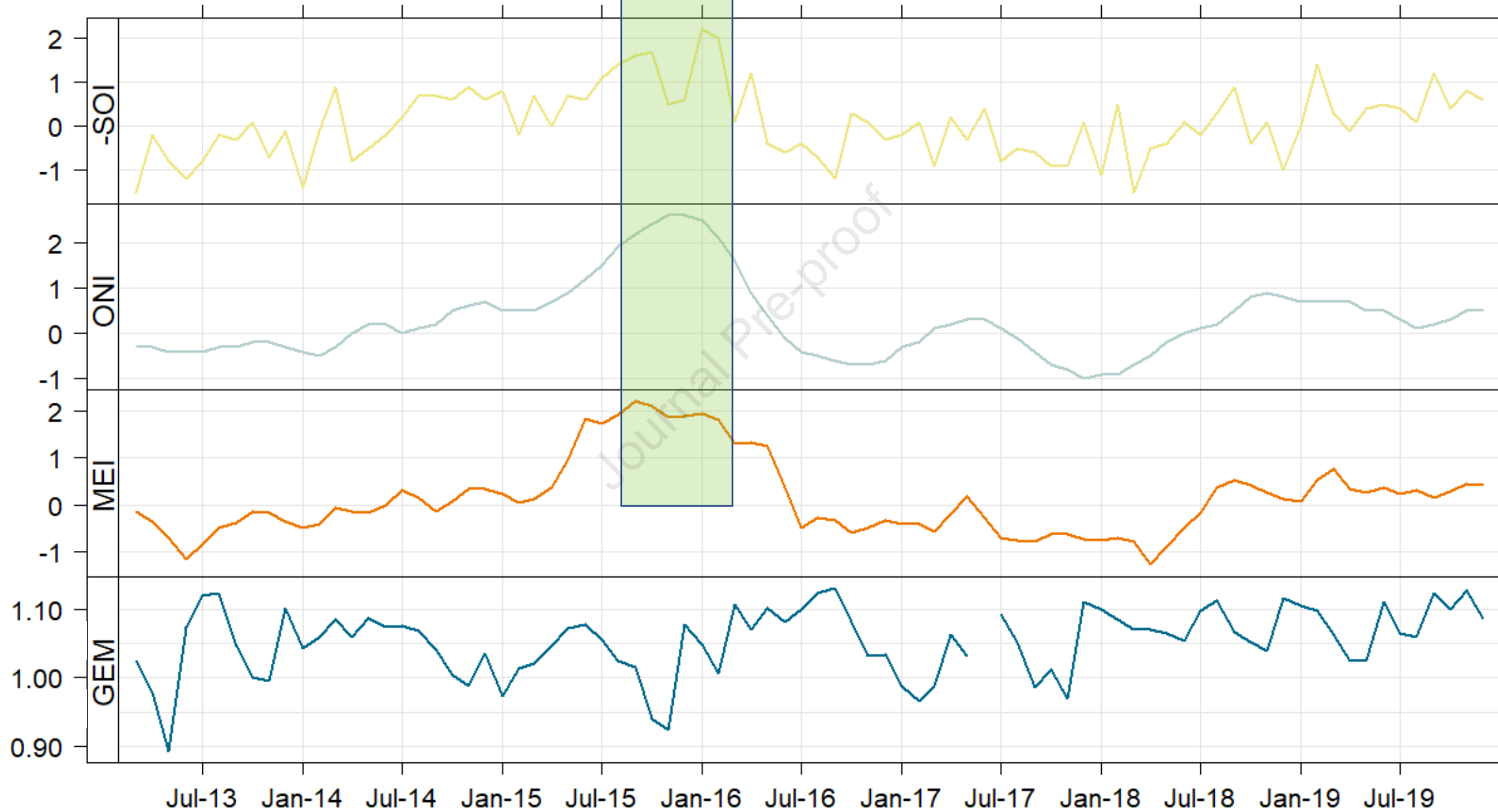


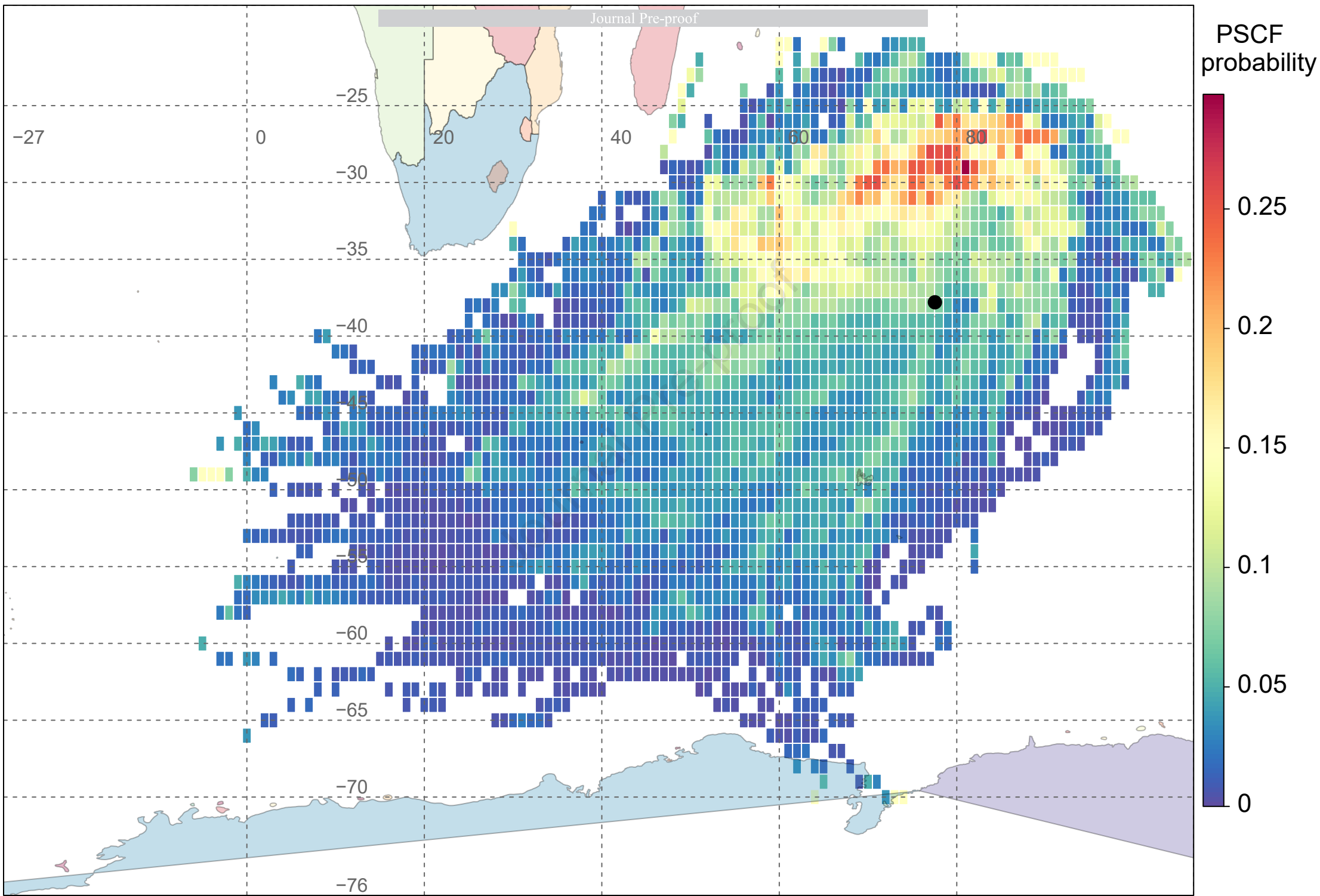
● VWMC
 ● rainfall





El Niño





Highlights

Gaseous Elemental Mercury at Amsterdam Island varied between 0.70 and 1.58 ng m⁻³

Total mercury concentration in wet deposition ranged from 1.16 to 4.67 ng L⁻¹

CO, CO₂, and CH₄ concentrations showed upward significant trends from 2013 to 2019

Gaseous Elemental Mercury was affected by El Niño-modulated biomass burning

Atmospheric mercury was governed by oceanic evasion and long-range transport

Journal Pre-proof